RESEARCH ARTICLE
ATMOSPHERIC PHYSICS

Earth and Planetary Physics
9: 925–937, 2025
doi: 10.26464/epp2025046

Inter-hemispheric couplings in the middle atmosphere exhibited by principal component analysis of the SD-WACCM-X simulations

Sheng-Yang Gu[1*], YuBo Zeng[1], Jin Hu[1], YuSong Qin[1*], Liang Tang[2], and YuXuan Liu[1]

[1]School of Earth and Space Science and Technology, Wuhan University, Wuhan 430072, China;

[2]School of Optoelectronic Engineering, Chongqing University of Posts and Telecommunications, Chongqing 400065, China

Key Points:

- The middle-atmosphere inter-hemispheric coupling (IHC) processes during wintertime in both hemispheres are investigated based on principal component analysis (PCA) of the 13-year SD-WACCM-X data.
- The IHC response during Southern Hemisphere (SH) winter is generally more complex and weaker than during Northern Hemisphere (NH) winter, primarily due to the weaker stationary planetary wave forcing in the SH stratosphere.
- The seasonal and spatial variation of IHC characteristics during NH winter may be more dependent on the quasi-two-day waves (QTDWs) activity compared to SH winter.

Citation: Gu, S.-Y., Zeng, Y. B., Hu, J., Qin, Y. S., Tang, L., Liu, Y. X. (2025). Inter-hemispheric couplings in the middle atmosphere exhibited by principal component analysis of the SD-WACCM-X simulations. *Earth Planet. Phys.*, *9*(4), 925–937. http://doi.org/10.26464/epp2025046

Abstract: This study employs Principal Component Analysis (PCA) and 13 years of SD-WACCM-X model data (2007−2019) to investigate the characteristics and mechanisms of Inter-hemispheric Coupling (IHC) triggered by sudden stratospheric warming (SSW) events. IHC in both hemispheres leads to a cold anomaly in the equatorial stratosphere, a warm anomaly in the equatorial mesosphere, and increased temperatures in the mesosphere and lower thermosphere (MLT) region of the summer hemisphere. However, the IHC features during boreal winter period are significantly weaker than during the austral winter period, primarily due to weaker stationary planetary wave activity in the Southern Hemisphere (SH). During the austral winter period, IHC results in a warm anomaly in the polar mesosphere of the SH, which does not occur in the NH during boreal winter period. This study also examines the possible influence of quasi-two-day waves (QTDWs) on IHC. We found that the largest temperature anomaly in the summer polar MLT region is associated with a large wind instability area, and a well-developed critical layer structure of QTDW in January. In contrast, during July, despite favorable conditions for QTDW propagation in the Northern Hemisphere, weaker IHC response is observed, suggesting that IHC features and the relationship with QTDWs during July would be more complex than during January.

Keywords: inter-hemispheric coupling; principal component analysis; middle atmosphere; quasi-two-day waves

1. Introduction

Inter-hemispheric coupling (IHC) refers to the phenomenon wherein the stratosphere above the winter hemisphere's polar region experiences warming or cooling. This leads to a corresponding warming or cooling in the upper mesosphere above the summer hemisphere's polar region, with a time delay of 2 to 10 days. Through a semi-spectral numerical model, Holton et al. (1983) identified that deviations observed in the middle atmosphere from radiative equilibrium, during both summer and winter, were primarily caused by gravity wave drag (GWD) and diffusion. Becker and Schmitz (2003), utilizing the SGCM model, observed cooling in the mesosphere linked to sudden stratospheric warming (SSW) events, additionally, a strong correlation was found between the thermal structure of the summer hemisphere's mesosphere and the stationary wave structure and thermal forcing in the winter hemisphere's troposphere, although the mechanism behind this cross-hemisphere coupling remained unexplained.

Becker et al. (2004) revisited the hypothesis of IHC in the mesosphere and proposed that the anomalous warming of the mesosphere, observed during the MaCWAVE/MIDAS campaign in the Northern Hemisphere (NH) summer of 2002, was potentially connected to the unusually warm stratospheric vortex in the Southern Hemisphere (SH) during the winter of 2002. The SGCM model was also run under July conditions with enhanced planetary wave thermal forcing, and produced a positive temperature response in the summer mesopause, which supports the hypothesis. Further research by Becker and Fritts (2006), using the KMCM model to simulate inertia-gravity waves generating drag in the mesosphere, revealed that summer mesosphere warming resulted from enhanced tropospheric forcing in the winter hemisphere. They noted that temperature anomalies in the high-latitude regions of the summer hemisphere were caused by distur-

Correspondence to: S.-Y. Gu, gushengyang@whu.edu.cn
Y. S. Qin, qinyusong@whu.edu.cn
Received 04 DEC 2024; Accepted 08 FEB 2025.
First Published online 11 APR 2025.

bances in GWD in the summer mesosphere. Thus, it was suggested that weakening GWD in the winter hemisphere leads to reduced cross-equatorial flow, weakening the summer easterly winds and accelerating the zonal wind through the Coriolis force, which drives the IHC process.

Karlsson et al. (2007), using OSIRIS data on noctilucent clouds (NLC) to represent summer hemisphere mesospheric temperatures, investigated whether IHC could be identified in observational data. The hypothesis posited that a warm polar stratosphere in the winter hemisphere correlates with a warm summer mesopause, and conversely, a cold winter polar stratosphere correlates with a cold summer mesopause. A strong negative correlation (with an absolute correlation coefficient greater than 0.9) was found between NLC occurrences, indicating cooler summer mesopause temperatures, and warmer winter stratospheric temperatures. Although limited to a five-year time series, the strength of the correlation provided strong empirical evidence for IHC.

Further research by Karlsson and McLandress (2009a), using an extended version of the CMAM model, revealed a robust positive correlation between winter polar stratospheric temperatures and summer polar mesopause temperatures. This correlation was driven by natural variability in planetary wave forcing during winter. The mechanism was confirmed to be linear, with anomalies in cross-equatorial flow induced by winter planetary wave forcing affecting GWD in the summer hemisphere. Differences of NLC occurrences between the NH and SH were also noted: in the SH, NLC exhibited greater variability, dimmer brightness, and earlier disappearance compared to the NH. These differences reflect the more active winter dynamics in the NH and the relatively stable dynamics of the SH.

Körnich and Becker (2010) proposed a simplified IHC mechanism characterized by necessary dynamical features described by an axisymmetric global mean circulation model with parameterized eastward and westward propagating gravity waves (GWS), excluding additional dynamical processes. Siskind et al. (2011) conducted a global weather analysis of the middle atmosphere using the NOGAPS-ALPHA forecasting/data assimilation system, demonstrating that the driving mechanisms of the temperature anomalies observed in July 2007 is the same as which proposed by Karlsson and McLandress (2009a) and Körnich and Becker (2010). Sato and Nomoto (2015) and Siskind and McCormack (2014) highlighted the significant role of in-situ wave forcing generated in the mesosphere and lower thermosphere (MLT) region of the middle atmosphere. France et al. (2018) indicated that cooling of the equatorial stratosphere often occurs during SSW events, where BC instability is enhanced by the strengthened westward jet in the summer stratosphere and middle atmosphere. Consequently, the westward forcing from increased QTDWs weakens the residual mean flow toward the equator, causing temperature anomalies near the polar summer mesopause. Becker and Vadas (2018) utilized a high-resolution KMCM model to investigate how primary gravity wave forcing in the winter middle atmosphere generates secondary GWs, which can propagate upward into the thermosphere and break at high latitudes. Yasui et al. (2018) demonstrated that the westward propagating GWs providing westward forcing in the summer MLT region are likely generated in situ due to shear instability, suggesting that secondary GWs in the MLT region likely contribute to the formation of warm anomalies during summer. Yasui et al. (2021) revisited the IHC associated with NH SSW events, proposing that the driving processes of IHC involve not only GWs and Rossby waves (RWs) from the troposphere, but also in-situ GWs, RWs, and Rossby-gravity waves (RGWs) generated in the middle atmosphere. They revealed the roles of various wave disturbances in the formation mechanism of IHC related to NH SSW events, finding that the in-situ generation of GWs and QTDWs is enhanced during events of equatorial stratospheric cooling, which elucidated the reasons for positive GW and QTDW forcing anomalies in the SH middle atmosphere. However, Smith et al. (2020) argued that wave forcing in the SH may not be significant for IHC, attributing the responses in the summer hemisphere MLT region to the transient responses of circulation induced by westward forcing, resulting from the breakup of winter stratospheric planetary waves, and driven by the zonal-mean mass balance of the atmosphere. Smith et al. (2022) investigated the coupling of circulation induced by wave forcing in the winter stratosphere between the NH and SH using satellite observations, concluding that the relationship between mid-latitude summer middle atmosphere temperature disturbances and summer stratospheric temperature disturbances is closer than that between mid-latitude summer middle atmosphere temperature disturbances and winter stratospheric wave forcing.

Due to the rarity of SSW events in the SH winter, and the limited sample size for studying IHC triggered by SH SSW events, previous research on IHC has predominantly focused on NH winters. Most studies (e.g., Karlsson and Randall, 2009b; Gumbel and Karlsson, 2011; Karlsson and Becker, 2016; Smith et al., 2020) suggest that the characteristics of IHC in SH winters are similar to those in NH winters. Smith et al. (2022) proposed that the temperature responses of SH IHC are weaker than those observed in NH winters. Significant differences in the characteristics of the middle atmosphere between the SH and NH (e.g., Ern et al., 2013; Rodgers and Prata, 1981; Iimura et al., 2021) may contribute to differing IHC characteristics and mechanisms between the two hemispheres during winter. Koshin et al. (2024) analyzed the structure and mechanisms of IHC triggered by stratospheric warming events in the SH winter using JAGAUR-DAS reanalysis data, comparing the differences in IHC between the two hemispheres with a particular focus on the role of QTDWs in IHC of Austral winter.

Previous studies on IHC were primarily based on traditional statistical and regression analysis methods, which requires directly analyzing datasets that contain a large amount of redundant information. Utilizing SD-WACCM data and employing principal component analysis (PCA), this study models and removes the background field and long-term trends of the middle and upper atmosphere. By analyzing the residual temperature fields, in which the amount of redundant information is relatively smaller and trends such as SSW are more conspicuous, the differences in IHC characteristics between the SH and NH are compared, and the reasons for these differences are diagnosed. The study also focuses on the impact of QTDWs activity on IHC characteristics and mechanisms in different hemispheres.

2. SD-WACCM-X Simulation

This study utilized SD-WACCM-X data driven by Whole Atmosphere Community Climate Model, version 4 (WACCM4). WACCM4 is an updated version of the Community Earth System Model (CESM), which also includes land, ocean, sea ice, and land ice components. The WACCM4 is established by the National Center for Atmospheric Research (NCAR), incorporating enhancements in physical, chemical, and aerosol parameterizations, and extending the model's vertical height into the middle atmosphere and lower thermosphere (up to 140 km). The model can reproduce observed climatology of temperature, wind, and trace gases such as water vapor and ozone in the middle atmosphere, as well as the stratospheric changes associated with SSW events, volcanic eruptions, and long-term trends. WACCM4 features three chemical mechanisms suitable for coupling: the troposphere-stratosphere (TS) mechanism, the middle atmosphere (MA) mechanism that reduces tropospheric reactions, and the middle atmosphere (MAD) mechanism incorporating D-region ionization chemistry. WACCM4 has been widely applied to study atmospheric fluctuations (planetary waves, gravity waves, etc.) during various SSW events, showing good agreement with other model simulations and observational results (e.g., Limpasuvan et al., 2012; Sassi et al., 2013; Qin YS et al., 2021). The WACCM-X model represents a designated dynamic version of WACCM4, further extending vertically into the thermosphere and ionosphere, with its upper boundary located at approximately 4.1×10^{-10} hPa (500–700 km). More detailed information about WACCM-X is described in Liu HL et al. (2018) and Liu HL et al. (2010).

This study employed the MERRA-2 reanalysis to constrain the model meteorology of WACCM-X (SD-WACCM-X), with a horizontal resolution of 1.9° × 2.5° (latitude × longitude) for experiments covering the time range from January 1st, 2007, to December 31st, 2019, at a temporal resolution of 24 hours, utilizing the MA mechanism for the selected processes. During simulations, the model is driven every 180 minutes by horizontal wind, temperature, and surface pressure data derived from meteorological assimilation analyses, to maintain adherence to actual dynamic conditions. The initial concepts and configurations of SD-WACCM-X are described in Marsh (2011).

3. Method

The principal component analysis (PCA, also known as EOF) is a data decomposition technique that represents the original data using a series of orthogonal basis functions and their corresponding correlation coefficients. This method can significantly reduce the dimensionality of the original dataset while maximizing the capture and retention of the variations present in the original dataset (Jolliffe, 2002). Compared to predefined orthogonal functions (such as spherical harmonics and Fourier functions), the basis functions in PCA are determined by decomposing the original dataset, such as by calculating the eigenvalues and eigenvectors of the covariance matrix, or through singular value decomposition. This allows the PCA sequence to preserve the original characteristics of the dataset, and the convergence of the characteristic sequences is rapid. To completely represent the original data, a series of basis functions and their corresponding correlation coefficients (hereafter referred to as modes) are required. In practical applications, a few primary modes are selected, which still represent the majority of the variation in the original dataset.

These advantages have made PCA one of the preferred methods for studying and analyzing temporal and spatial changes in the field of meteorology. Dvinskikh (1988) provided a detailed introduction to the PCA method and its preliminary applications in ionospheric modeling. Studies by Liu JB et al. (2017), Wan WX et al. (2012) have extensively applied PCA in simulating ionospheric and surface temperature phenomena.

The atmospheric temperature data simulated by SD-WACCM-X from 2007 to 2019 were processed with zonal averaging on different latitude circles, and interpolation was performed at a height resolution of 2 km, resulting in atmospheric temperature data within a latitude range of 88°S to 88°N and a height range of 10 to 120 km. To eliminate smaller disturbances on both time and spatial scales, facilitating subsequent modeling and research on IHC, the temperature data underwent a sliding average using a 6 km height window, followed by another sliding average with a 30-day time window, completing the data preprocessing. Subsequently, the atmospheric temperature was re-expressed as a function of height and date, where the daily atmospheric temperature is denoted as T, with h and t representing height and date, respectively. The decomposition is performed using time-independent basis functions (hereafter referred to as PC) and time-dependent coefficients, resulting in an optimized form:

$$T(h,t) = \sum_{i=1}^{n} a_i(t)\, PC_i(h). \tag{1}$$

The amplitude of a_i is determined by the inner product of T with the PC_i. The PC_i are orthogonal and normalized and obtained through PCA, while satisfies the following equation:

$$\boldsymbol{S} \times PC_i = \beta_i PC_i. \tag{2}$$

In the equation, S represents the covariance matrix, obtained by $\boldsymbol{S} = \boldsymbol{T}^{\mathrm{T}}\boldsymbol{T}$. β_i and PC_i are the eigenvalues and eigenvectors, respectively, obtainable through eigenvalue decomposition. It is important to note that PC_i are normalized, with their order corresponding to the order of the respective eigenvalues β_i. β_i are sorted by variance contribution $\frac{\beta_i}{\sum_{j=1}^{n}\beta_j}$ from largest to smallest. After obtaining the basis functions, the corresponding time-dependent amplitudes $a_i(t)$ for each PC component in the SD-WACCM-X atmospheric temperature data from 2007 to 2019 can be calculated using the following formula:

$$a_i(t) = T(h,t) \times PC_i. \tag{3}$$

The resulting $a_i(t)$ are then parameterized and fitted according to the following fitting formula:

$$a_i = B_{SA} B_{\mathrm{time}}. \tag{4}$$

Where B_{SA} represents the influences of solar activity and geomagnetic activity while B_{time} indicate annual and semiannual oscillations, B_{SA} and B_{time} are expressed as follows:

$$B_{SA} = (a_1 F_{10.7} + a_2) \times (a_3 Ap + a_4), \tag{5}$$

$$B_{\mathrm{time}} = c + \sum_{k=1}^{2} \left(m_{1k} \sin\frac{2\pi kd}{365} + m_{2k} \cos\frac{2\pi kd}{365}\right). \tag{6}$$

Here, $F_{10.7}$ denotes the daily 10.7 cm solar radiation flux, Ap represents the daily average geomagnetic activity Ap index, and a_1, a_2, a_3, a_4, m_{1k}, m_{2k}, c represent constant terms, while d represents the day number in the year starting from January 1st. The modeling process is completed by multiplying the fitted amplitudes $B_{SA}B_{\mathrm{time}}$ with the basis functions PC_i. In this study, the first seven modes are selected at different latitudes, with their combined variance contribution exceeding 99.95%, utilizing these modes to model the original atmospheric temperature data. The modeling results are illustrated in Figure 1, which compares the original temperature data at 1°S, the modeling results, and the residuals between the original data and the modeling results. Figure 1a displays the preprocessed original atmospheric temperature data at 1°S. Figure 1b shows the modeling results using PCA with the first seven modes, which effectively replicate most of the variation trends in the original temperature field compared to the original data. Figure 1c illustrates the distribution of residuals between the original data and the modeling results, with residual values ranging from −8 K to 10 K. Compared to the original data, the modeling results exhibit deviations within 6%, and the residuals clearly reveal subtle variations, such as the quasi-biennial oscillation, which are less prominent in the original data.

4. Results and Discussion

Before presenting the results of this study, it is essential to outline the basic principles of wave-driven mean circulation in the middle atmosphere and the IHC mechanism. The wave-driven circulation described by Körnich and Becker (2010) corresponds to the average trajectory of air parcels (Dunkerton, 1978) and is primarily driven by the zonal forces generated by the breaking of GWs and planetary Rossby waves (Holton and Alexander, 2000). The eastward winds in the summer stratosphere and westward winds in the winter stratosphere play a critical role in this process. Planetary Rossby waves, being quasi-stationary, can propagate vertically into the winter stratosphere, but are blocked from entering the summer stratosphere. On the other hand, GWs, which have either eastward or westward zonal phase speeds, encounter a critical layer and break when their phase speed matches the background wind speed (Fritts et al., 2003), causing a deposition of momentum in the direction of their phase speed. Therefore, the background

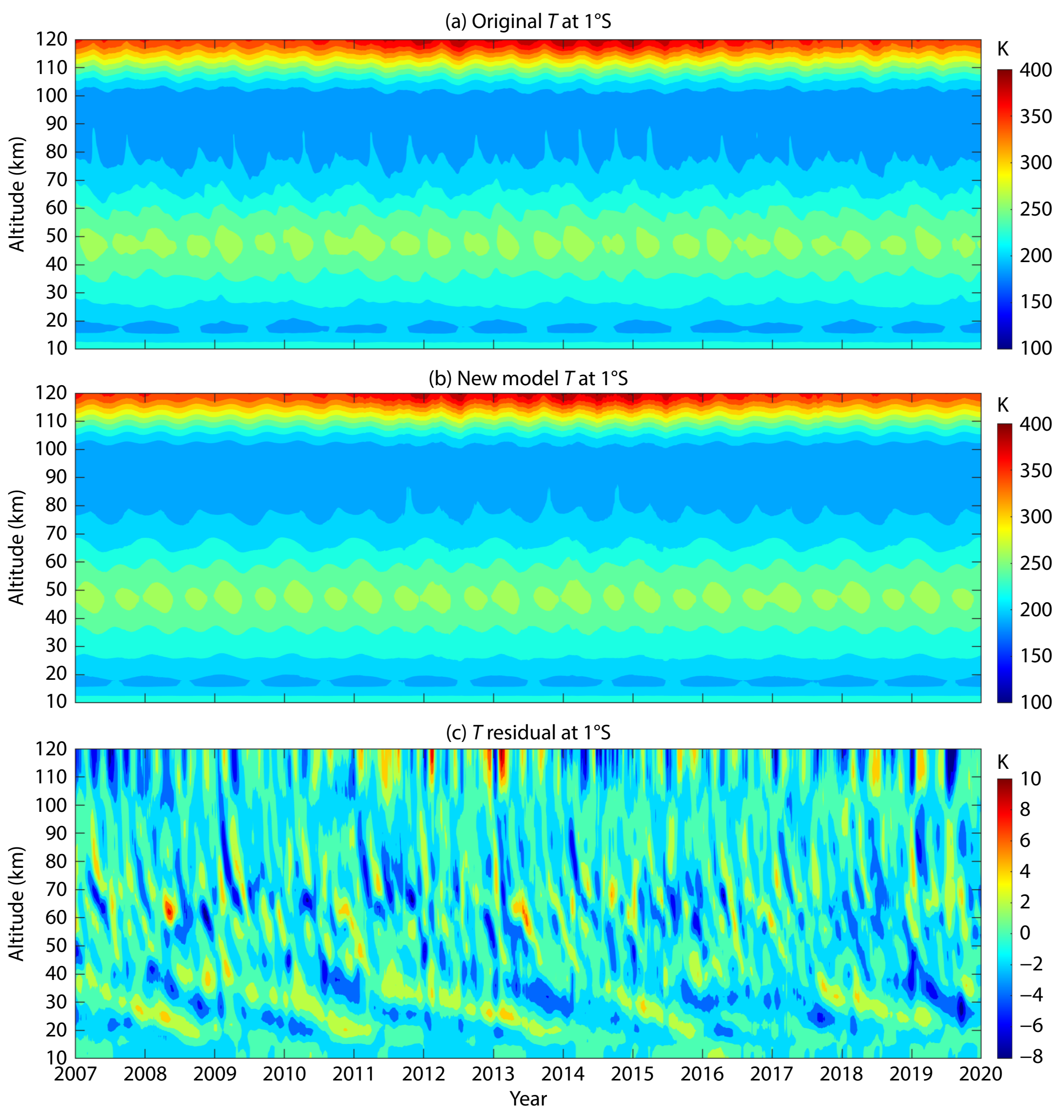

Figure 1. Comparison of (a) original atmospheric temperature, (b) modeled atmospheric temperature using PCA, and (c) residuals.

wind in the stratosphere favors the vertical propagation of GWs with phase speeds opposite to the wind. In the mesosphere, the momentum deposition from GWs produces a zonal drag in the direction of the wave's phase speed, acting on the zonal mean flow. Due to the filtering effect of the stratosphere, the upper summer mesosphere generally experiences positive GWD, while the winter mesosphere experiences negative GWD. This GWD forces a cross-equatorial circulation, maintaining a balance between the summer and winter hemispheres, with upward motion in the summer mesosphere and downward motion in the winter mesosphere, leading to strong deviations from radiative equilibrium in the temperature fields.

The IHC mechanism unfolds in several steps. First, an anomaly in stationary planetary wave drag (PWD) occurs in the winter hemisphere stratosphere, which induces a Brewer-Dobson circulation. According to the downward control principle (Haynes et al., 1991), this anomalous circulation leads to a warmer winter stratosphere and a cooler tropical stratosphere (Yulaeva et al., 1994), weakening the polar vortex. In some extreme SSW events, the weakening of the polar vortex may even cause the stratospheric winds to reverse, generating eastward winds. The weakened winter stratospheric jet alters the filtering of gravity waves, allowing more eastward-propagating GWs to reach the mesosphere, reducing westward GWD. This reduction in westward drag drives an anomalous meridional circulation towards the equator, suppressing the usual mean circulation. This circulation anomaly, according to the downward control principle, results in a cooling of the winter polar mesosphere and warming in the tropical mesosphere.

Next, the effects of the winter hemisphere anomalies propagate across the equator to influence the summer hemisphere. Karlsson et al. (2009a) suggested that the mechanism is based on the warming of the tropical mesosphere, which increases the meridional temperature gradient in the summer hemisphere. Due to the principle of thermal wind balance, this leads to an acceleration of the subtropical zonal winds in the summer hemisphere. Since there is no significant change in the zonal wind in the summer stratosphere and troposphere, the gravity wave filtering process remains unchanged, allowing only GWs with sufficiently large eastward phase speeds to propagate into the mesosphere. However, due to the increase in zonal wind speed in the mesosphere, the background wind speed becomes closer to the phase speed of the GWs, increasing the vertical wave-number of GWs and lowering the altitude at which the waves break. This causes the GWD to shift downward, lowering the altitude of the mean circulation, leading to a positive temperature response in the summer polar mesosphere.

In addition, the positive temperature anomaly observed in the summer polar mesosphere and lower thermosphere is believed to be driven by the forcing of QTDWs and secondary GWs. Plumb (1983) suggested that QTDWs radiate from regions in the summer mesosphere where the meridional gradient of potential vorticity (PV) is negative, which is a necessary condition for barotropic/baroclinic (BT/BC) instability. The westward forcing induced by QTDWs weakens the meridional flow toward the equator in the summer mesosphere, leading to a warm anomaly in the summer polar region (e.g., Siskind and McCormack, 2014). Yasui et al. (2018) proposed that shear instability, caused by primary GW forcing in the upper part of the summer easterly jet, generates westward-propagating secondary GWs, which provide westward forcing in the MLT region and contribute to the positive temperature anomaly in the summer polar region.

Due to significant differences in stratospheric stationary planetary wave activity (e.g., Andrews et al., 1987), the frequency of SSW events (e.g., Chandran et al., 2014), and the amplitude of QTDWs (e.g., Ern et al., 2013), it is evident that there are marked distinctions in the characteristics of the middle atmosphere between the SH and NH (Iimura et al., 2021; Rodgers and Prata, 1981). These differences may result in variations in the characteristics and mechanisms of warm anomalies during the winter seasons of the SH and NH. This study first discusses the differences in IHC between the SH winter and NH winter.

For this study, the zonal mean temperature at 70°N and 10 hPa from 2007 to 2019 was selected to represent the intensity of SSW events in the NH over the 13- year period, denoted as SSW70°N. Similarly, the zonal mean temperature at 70°S and 10 hPa was selected to represent the intensity of SSW events in the SH, denoted as SSW70°S. The global responses associated with the two indices mentioned above are examined separately. The modeling procedure described earlier was applied to all 94 latitudes between 88°S and 88°N, with a latitude spacing of 1.9°. To better compare the similarities and differences in IHC between the NH and SH, this study calculated the residuals between the original and modeled data for the periods from December to February (NH winter) and June to August (SH winter) over the 13-year period. Correlation analyses were conducted at different altitudes with respect to SSW70°N and SSW70°S, and the summarized results are shown in Figure 2.

Figure 2a shows the average distribution of the atmospheric temperature modeling residual's response to SSW70°N, as a function of latitude and altitude, during the NH winter from December to February over the 13-year period. The largest positive response to SSW70°N occurs between 50°N and 88°N, and below 50 km in altitude, with peak values reaching 0.99. A broad negative response is observed between 10°S and 10°N latitude, and at altitudes of 20–50 km, with peak values around −0.8. This is consistent with the anomalously warm winter stratosphere and the cooling of the tropical stratosphere caused by the Brewer-Dobson circulation, channeled by stationary planetary wave drag anomaly (Yulaeva et al., 1994). Additionally, a strong positive response is seen at altitudes of 60–90 km, between 10°S and 10°N latitude, with peak values near 0.6. A clear negative response is observed between 40°N and 88°N at altitudes of 50–90 km, with peak values exceeding −0.8. This corresponds to the warming of the equatorial mesosphere and the cooling of the polar mesosphere, driven by the anomalous meridional circulation induced by eastward-propagating GWs. A positive response is also seen between 50°S and 88°S at altitudes of 85–110 km, with most values around 0.6 and peaks reaching 0.8 corresponding to the temperature increase in the summer polar mesopause and lower thermosphere, might be caused by the downward shift of the residual circulation (Karlsson et al., 2009a). However, it might also be caused by QTDWs and secondary GWs, providing westward forcing

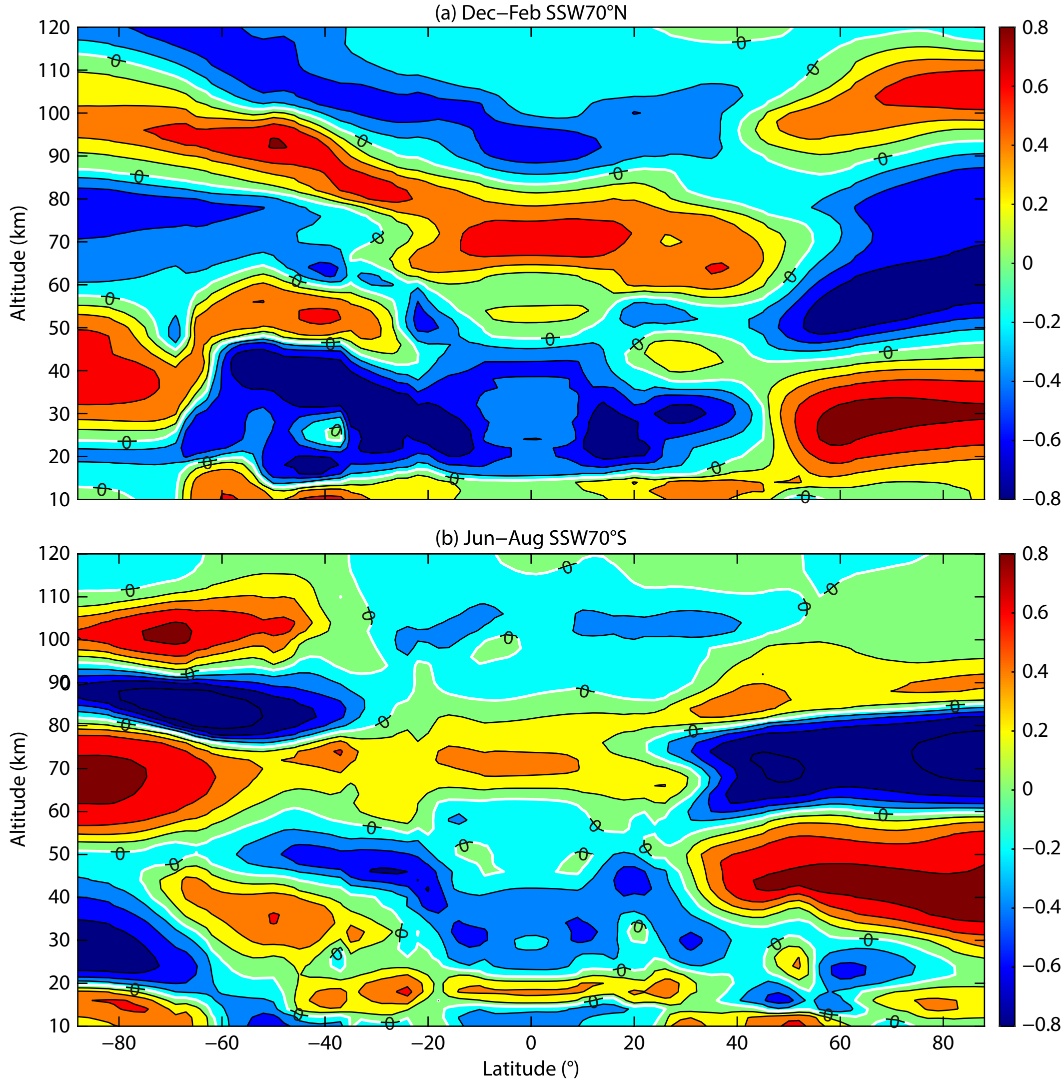

Figure 2. Average response of temperature modeling residuals to SSW70°N during the NH winter (a) and average response of temperature modeling residuals to SSW70°S during SH winter (b) from 2007 to 2019.

(Yasui et al., 2021).

Figure 2b shows the average distribution of the temperature modeling residual's response to SSW70°S during the SH winter (June to August). A positive response, with values around 0.4, is observed between 40°S and 70°S below 50 km. Compared to the NH winter response in the same altitude range, which is also caused by the stationary planetary wave drag anomaly, the SH winter response is weaker and more concentrated in the mid-latitudes. This is because SSW events are less frequent in the SH winter and tend to occur in the mid-latitudes, unlike the NH, where they primarily occur in the high latitudes (Koshin and Sato, 2024). Additionally, a strong positive correlation, with peak values reaching 0.8, is seen between 70°S and 88°S at altitudes of 55–80 km, a response that is unique to the SH winter. This is due to the enhanced meridional temperature gradient in the SH mid-latitudes, leading to the intensification and pole-ward shift of the polar vortex, which enhances the filtering of eastward-propagating GWs, reducing eastward momentum deposition in the mesosphere and generating anomalous westward forcing. This westward forcing strengthens the polar-ward circulation between 60°S and 90°S, and, according to the thermal wind balance, results in a warm anomaly in the high-latitude region of the SH (Koshin and Sato, 2024). A negative response with peak values around −0.5 is observed between 10°S and 10°N at altitudes of 25–50 km, while a positive response with peak values around 0.4 is seen in the same latitude range at altitudes of 60–85 km. These responses are similar to those observed in the same region in NH winter, but weaker. Moreover, a positive response is observed between 50°N and 88°N at altitudes of 85–100 km, resembling the response in the SH polar-side MLT region during December to February shown in Figure 2a. Notably, this response is also weaker compared to that of the NH winter. These similar-to-but-weaker-than-NH-winter's responses are also related to the weaker and less frequent occurrence of SSW events during the austral winter compared to the boreal winter, consistent with the findings of Smith et al. (2022).

Next, this study conducts a diagnostic analysis of the impact of inter-hemispheric differences in stationary planetary wave activity on the characteristics of IHC between the NH and SH.

It is well known that stationary planetary wave-1 (SPW1) is the main cause of winter polar vortex distortion, which can trigger SSW events (Manney et al., 1994). Therefore, this paper uses SPW1 as an indicator of stationary planetary wave intensity in the winter hemisphere. Figure 3a shows the mean state of SPW1 at 20 hPa for the NH winter (December–February) over the 13-year period from 2007 to 2019, while Figure 3b presents the same for the SH winter (June–August) at 20 hPa over the same period.

In Figure 3a, it can be seen that NH winter stationary planetary wave activity is strong between 40°N and 80°N, particularly from day 335 of the year to day 40 of the following year (corresponding to December through late January or early February), with amplitudes reaching up to 1400 meters. In Figure 3b, SH winter stationary planetary wave activity is strong between 40°S and 80°S from day 195 to day 250 (corresponding to mid-July through late August), with amplitudes peaking at 1100 meters. Comparatively, the SH winter stationary planetary waves are weaker than those in the NH, and this is consistent with Figure 2, which shows that the tropical stratospheric cold anomalies and tropical mesospheric warm anomalies during the SH winter are weaker than those in the NH, and similarly, the NH summer polar-side MLT region exhibits weaker warm anomalies than the SH. This indicates that SH winter IHC is generally weaker than NH winter IHC.

Additionally, this study focuses on the seasonal variations of IHC characteristics and mechanisms during the NH winter and SH winter, and conducts diagnostic analysis of the variations in the summer hemisphere based on the intensity of QTDWs activity.

Based on Gu SY et al. (2016a, 2016b), the propagation and amplification of QTDWs can be represented by regions of background flow instability. These regions of instability are areas where the background wind is unstable, and such instability can amplify planetary waves through wave-mean flow interactions. The amplification occurs most frequently at the critical layer, where the phase speed of the wave (c) equals the zonal wind speed ($\overline{u}$) of the background flow. The regions of flow instability are quantified by the negative latitudinal gradient of quasi-geostrophic potential vorticity ($\overline{q}_\varphi$) (Andrews et al., 1987):

$$\overline{q}_\varphi = 2\Omega\cos\varphi - \left(\frac{(\overline{u}\cos\varphi)_\varphi}{a\cos\varphi}\right)_\varphi - \frac{a}{\rho}\left(\frac{f^2}{N^2}\rho\overline{u}_z\right)_z, \tag{7}$$

where the subscripts φ and z represent latitude and vertical gradients, respectively, and a, f, N, ρ, and Ω are the earth's radius, Coriolis parameter, Brunt-Väisälä frequency, background air density, and Earth's angular velocity, respectively.

To investigate the impact of temporal variations of QTDWs during summer in different hemispheres on the IHC, this study presents the average responses of the modeled temperature field residuals for December, January, and February to SSW70°N, as well as for June, July, and August to SSW70°S from 2007 to 2019. Diagnostic analysis was conducted using the $\overline{q}_\varphi$.

Figure 4 shows the average atmospheric temperature modeling residual's response to SSW70°N during SH summer months (December, January, and February) over the 13-year period from 2007 to 2019. In December and January, a negative response, indicating a colder equatorial stratosphere, is observed between 20°S and 20°N latitude and at altitudes of 20–50 km, with peak values exceeding −0.8. At the same latitude, but altitudes of 60–90 km, a positive temperature response is observed, representing a warm equatorial mesosphere, with peak values around 0.75. While in February, the similar responses weaken, with a smaller negative response in the equatorial stratosphere, peaking at about −0.4, and a weaker positive response in the equatorial mesosphere, peaking at about 0.65. This is consistent with the results shown in Figure 3a, where the stationary planetary wave activity in the NH is stronger in December and January but weaker in February. Moreover, Figure 4 indicates a positive response in January within the altitude range of 20–50 km and latitude range of 50°N–88°N, with a peak of approximately 0.8. The positive responses in the same region during December and February are weaker than in January. Similarly, a negative response at the same latitude range

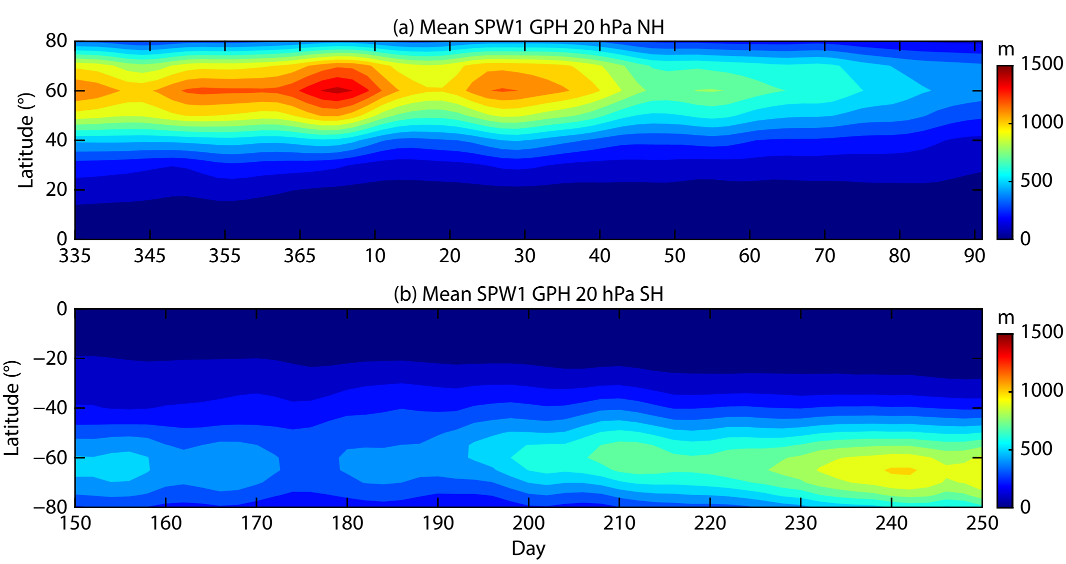

Figure 3. The average amplitude of stationary planetary wave (SPW) with zonal wave-number 1 (SPW1) at 10 hPa in (a) NH and (b) SH during winter of 2007–2019. The x-axis represents the day of year and the y-axis denotes latitude.

and at altitudes of 50–90 km also reaches its strongest point in January, with a peak exceeding −0.8. This pattern also aligns with the stationary planetary wave activity shown in Figure 3, where stationary planetary wave activity in the Northern Hemisphere during winter peaks between day 0 and day 30 of the year (corresponding to January), with maximum amplitudes reaching up to 1400 m.

Additionally, in January, a strong positive response is observed in the SH polar-side MLT region, with peak values reaching 0.7, while in December and February, the positive response in the same region is weaker, with values around 0.1 and 0.4, respectively.

Figure 5 shows the average state of background flux instability and critical layer In SH summer (December, January and February) over the 13-year period from 2007 to 2019. In Figure 5, unstable regions ($\overline{q}_{\varphi} < 0$) are shown in blue, while the critical layers ($\overline{u} - c < 0$) for QTDWs are marked by green solid lines. In December, January, and February, two unstable regions are observed: one at mid-latitudes (10°S to 40°S, 50–80 km), and the other at high latitudes (60°S to 88°S, 50–90 km). However, while critical layers are present in both regions during December and January, the critical layer at mid-latitudes disappears in February. Furthermore, compared to December, the critical layer and unstable region in the mid-latitudes of the SH in January are larger, with the critical layer extending through the unstable region. This structures of the critical layer and unstable region can better enhance the in-situ generation of QTDWs, and is also better for the propagation and amplification of QTDWs. The QTDWs reaching the critical layer through unstable regions undergo excessive reflection, providing additional amplification for the growth of planetary waves (Liu HL et al., 2004). Considering that the divergence of Eliassen-Palm (EP) flux from QTDWs has been shown to dominate the decomposed large-scale wave spectrum, and to oppose the GWD forcing in the summer hemisphere (McLandress et al., 2006; Pendlebury, 2012)，it is believed that the amplified QTDWs with westward phase speed propagate upward, accumu-

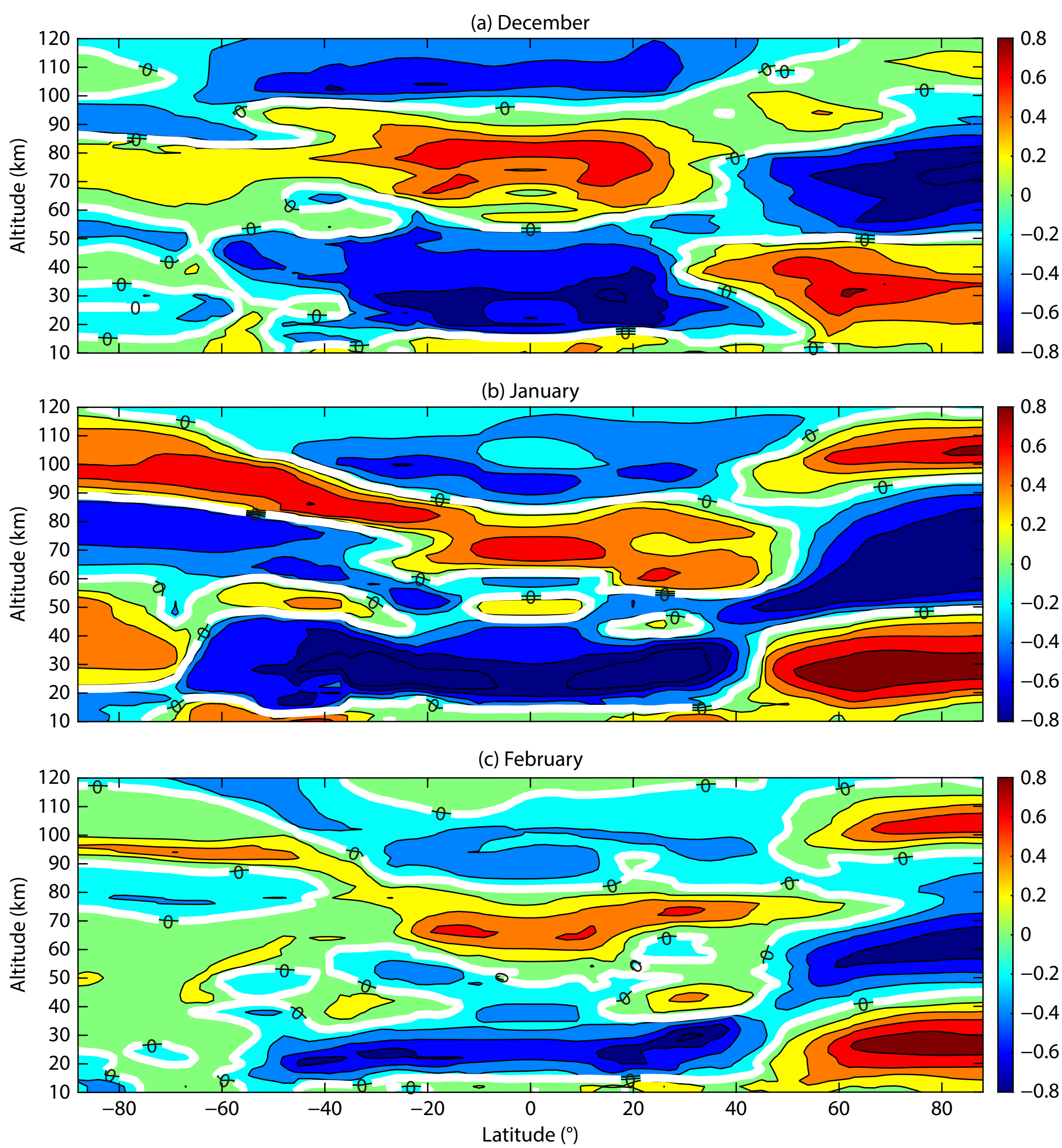

Figure 4. Average response of temperature modeling residuals to SSW70°N during the SH summer ((a) December, (b) January, (c) February) from 2007 to 2019.

lating westward momentum at the mesopause and lower thermosphere, leading to westward forcing and weakening of the equatorward flow in the summer mesosphere, ultimately resulting in warm anomalies in the summer polar region, which align with the strongest warm anomaly in the summer polar MLT region, observed in January as seen in Figure 4.

Figure 6 shows the average temperature modeling residual's response to SSW70°S during the NH summer (June, July, and August) over the 13-year period from 2007 to 2019. Compared to the inter-equatorial coupling characteristics presented in Figure 4 for the SH summer, the inter-equatorial coupling features in the NH summer are more complex, and exhibit greater inter-monthly variability, which may be due to the significantly lower intensity of stationary planetary wave activity compared to the NH, as shown in Figure 3, resulting in IHC processes of the SH that are more susceptible to the combined influence of multiple factors. It shows that during June, July, and August, strong negative correlations appear at latitudes 20°S to 20°N, and heights of 30–50 km, with amplitudes around −0.5. In July, a strong positive correlation response is observed in the latitude range 20°S to 20°N, and height range 60–90 km, with peak values exceeding 0.6. Additionally, slight positive correlations around 0.5 are noted in the same latitude range for heights of 65–75 km during June and August.

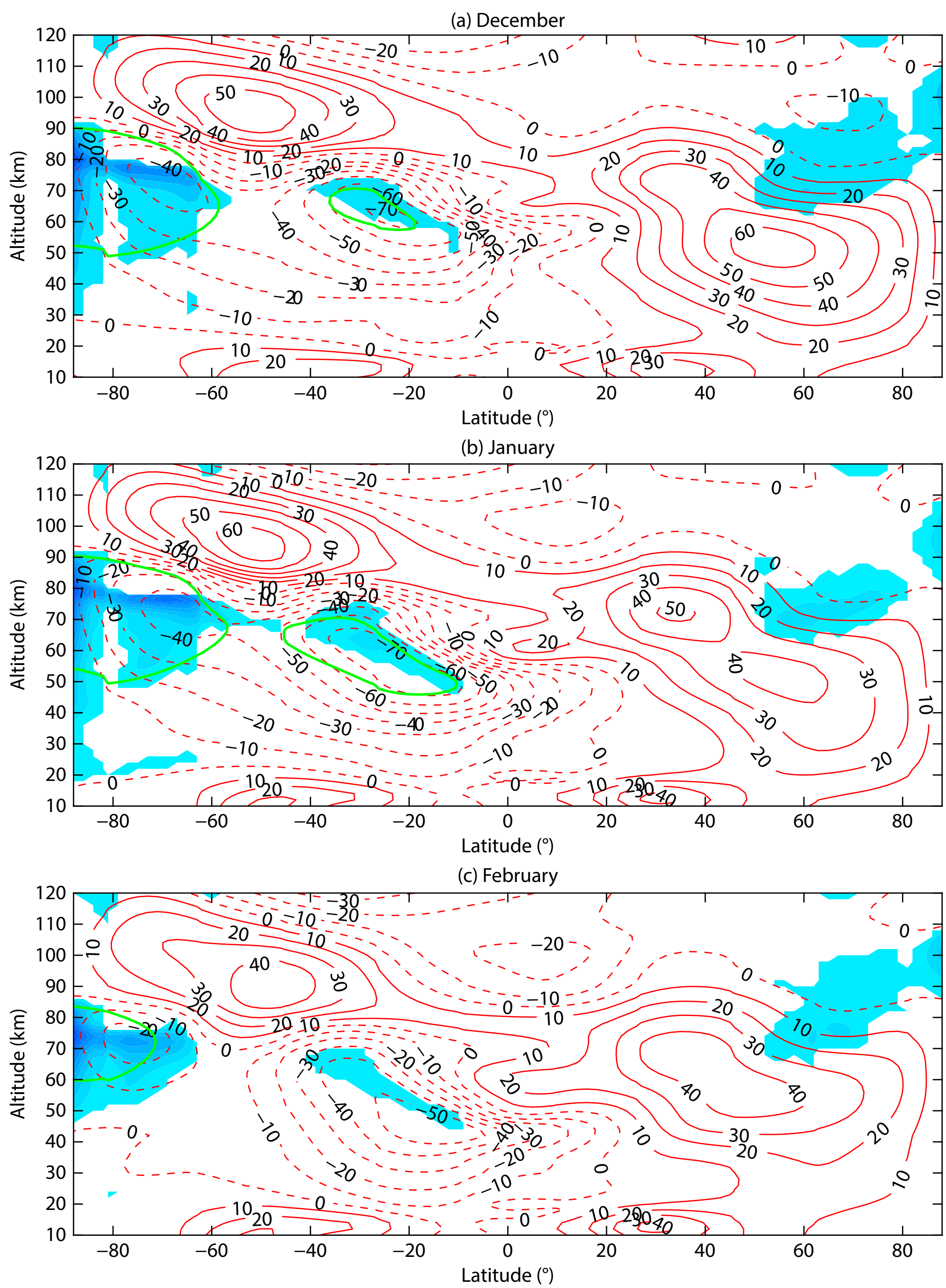

Figure 5. Average state of the critical layer of QTDWs and background flow instability during the summer ((a) December, (b) January, (c) February) in SH.

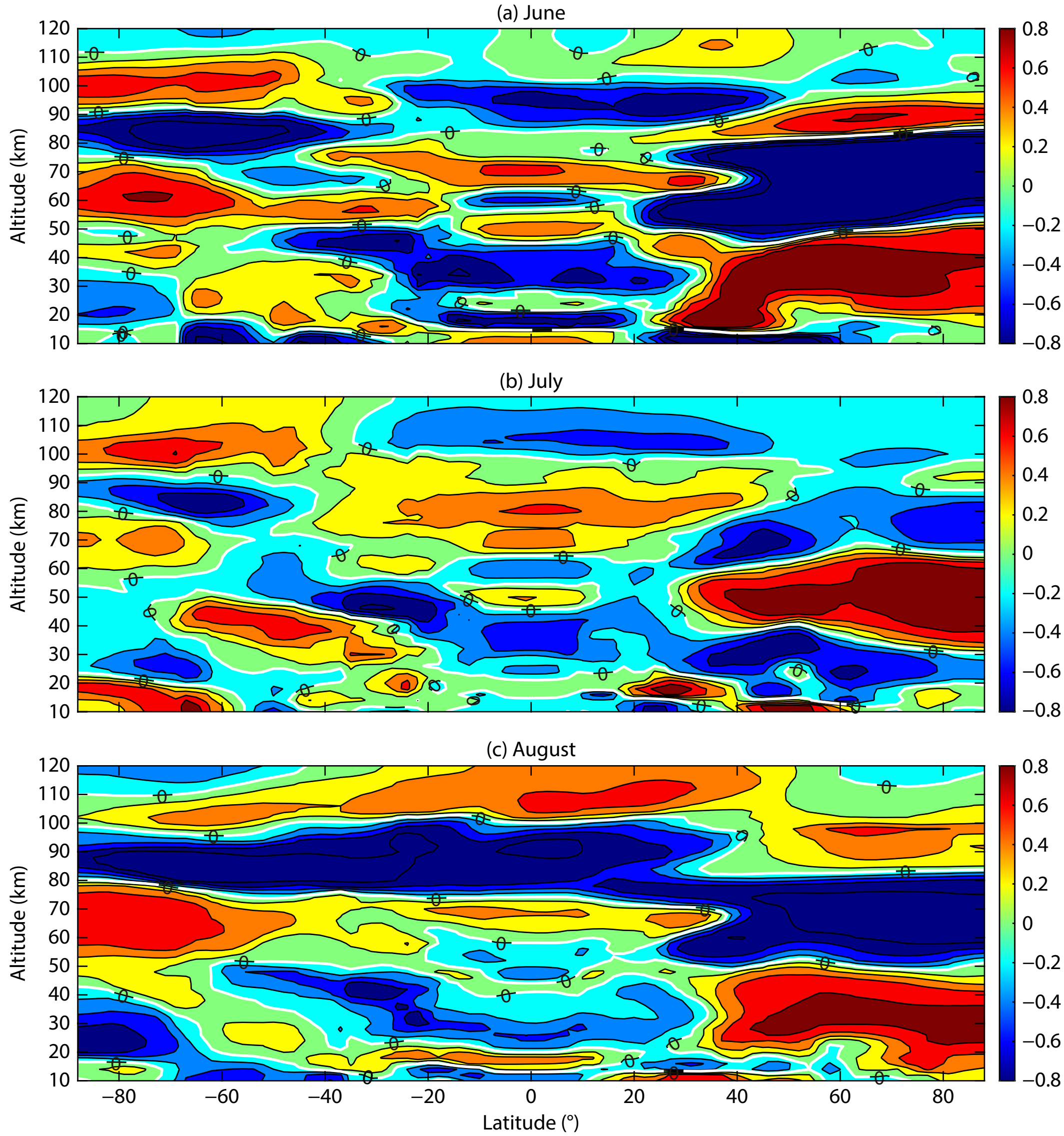

Figure 6. Average response of temperature modeling residuals to SSW70°S during the NH summer ((a) June, (b) July, (c) August) from 2007 to 2019.

The MLT region at latitudes 60°N to 88°N exhibits its strongest positive response to SSW70°S in August, with the maximum positive response in June reaching 0.8, albeit limited to a small height range of 85–95 km. In contrast, August displays a generally stronger positive response above 85 km at the same latitudes. For July, a peak positive response of 0.2 is only observed at latitudes 70°N to 88°N and heights of 90–100 km.

The average flux instability for NH summer (June, July, and August) from 2007 to 2019 is illustrated in Figure 7, with unstable regions highlighted in blue and the critical layer of QTDWs covered by solid green lines. It is evident that in June, July, and August, unstable regions are found in August and July at latitudes 20°N to 60°N, and altitudes 60–80 km, while in June, the unstable region appears only at latitudes 32°N to 45°N, and altitudes 65–75 km. Compared to August, when critical layers appear both at mid-latitude and high-latitude unstable regions in the NH, the mid-latitude unstable region in June lacks critical layers and is much smaller than the mid-latitude unstable region in August. The larger unstable region and more complete critical layer structure extending through the unstable region in August are more conducive to the generation, propagation, and amplification of QTDWs. Consequently, the stronger westward forcing induced in the mesosphere and MLT region by a greater number of higher-amplitude QTDWs leads to more pronounced warm anomalies in the summer polar region. This aligns with the observation in Figure 6 that the positive response in the summer polar-side MLT region in August is greater than that in June.

Additionally, compared to August, the critical layer in the NH mid-latitudes in July is larger; however, the warm anomaly response at the MLT region at the summer polar side in July shown in Figure 6b is quite smaller than in June and August. This may be attributed to the SD-WACCM-X model's poor simulation of QTDWs activity in July, while the strong positive response at the same region in June, shown in Figure 6a, may result from secondary GWs dominating as the cause of summer hemisphere warm anomalies during the IHC process in June.

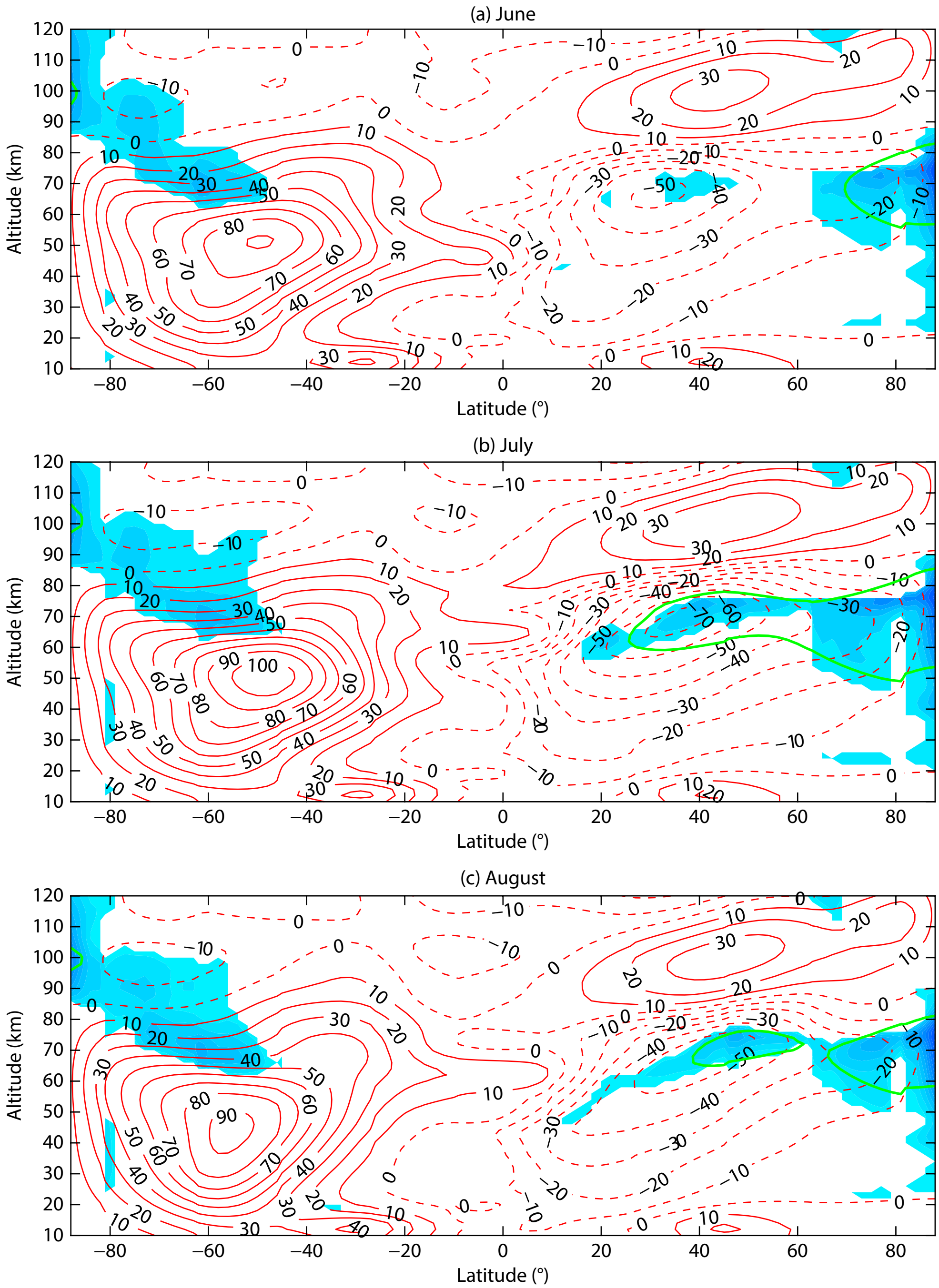

Figure 7. Average state of critical layer of QTDWs and background flow instability in the NH summer ((a) June, (b) July, (c) August) from 2007 to 2019.

5. Conclusion

This study utilized SD-WACCM-X data and PCA to investigate IHC within the middle atmosphere. The analysis emphasized significant differences in IHC between the NH and SH, particularly during their respective winter seasons. Diagnostic analysis revealed that these differences are closely related to varying stratospheric stationary planetary wave activity and QTDWs activity between the two hemispheres.

The revealed differences in IHC between the two hemispheres include a more complex IHC mechanism during the SH winter compared to the NH winter, with the SH generally exhibiting a weaker IHC response，because the intensity of stationary planetary waves in the SH during winter is less than that in the NH. Dramatic stratospheric warming during the SH winter predominantly occurs in mid-latitude regions, whereas in the NH, it takes place mainly in high-latitude areas. Additionally, a strong positive temperature correlation is observed in the polar mesosphere during the SH winter, which is absent in the NH.

Furthermore, this research explored the seasonal variations of QTDW activity in both hemispheres during summer, as well as their impacts on IHC characteristics and mechanisms. Results indicate that QTDWs play a crucial role in driving positive temperature anomalies in the polar middle and lower thermosphere during summer. The seasonal variation of QTDWs activity further contributes to the differences in IHC mechanisms. In January, the SH exhibits the strongest positive temperature response in the polar MLT region, coinciding with a larger background flow instability region and a complete critical layer extending through the unstable region. In August, the NH shows the strongest positive temperature response in the polar MLT region, characterized by a larger background flow instability region and a more complete critical layer. However, the optimal unstable regions and critical layer structures for QTDWs propagation and amplification in July do not manifest in the IHC response for that month, potentially due to suboptimal simulation of July QTDWs by the SD-WACCM-X. Additionally, although the background flow instability region and critical layer in June are smaller compared to July and August, a strong positive temperature response is still observed in the polar MLT region during June, likely dominated by westward forcing from secondary GWs and the descending residual circulation at vertical heights during that month.

Data Availability Statement

The $F_{10.7}$ solar index and *Ap* index can be accessed via https://omniweb.gsfc.nasa.gov/form/dx1.html. The WACCM-X is open-source software, and its source code can be accessed publicly at https://escomp.github.io/CESM/releasecesm2/downloading_cesm.html#downloading-the-code-and-scripts. The atmospheric forcing data, regridded from the MERRA -2 data set and used to run SD-WACCM-X, is available at https://rda.ucar.edu/datasets/ds313.3/?hash=access. The numerical calculations in this paper have been conducted on the supercomputing system in the Supercomputing Center of Wuhan University.

Acknowledgements

This research was supported by the National Natural Science Foundation of China (Grant Numbers 42374195 and 42188101), the fellowship of China National Postdoctoral Program for Innovative Talents (Grant Number BX20230273), the Hubei Provincial Natural Science Foundation of China (Grant Number 2024AFB-097), and the Postdoctor Project of Hubei Province (Grant Number 2024HBBHCXA054).

References

Andrews, D. G., Holton, J. R., and Leovy, C. B. (1987). *Middle Atmosphere Dynamics* (pp. 489). Orlando: Academic Press.

Becker, E., and Schmitz, G. (2003). Climatological effects of orography and land–sea heating contrasts on the gravity wave–driven circulation of the mesosphere. *Circulat. Mesosph.*, *60*(1), 103–118. https://doi.org/10.1175/1520-0469(2003)060<0103:CEOOAL>2.0.CO;2

Becker, E., Müllemann, A., Lübken, F. J., Körnich, H., Hoffmann, P., and Rapp, M. (2004). High Rossby-wave activity in austral winter 2002: Modulation of the general circulation of the MLT during the MaCWAVE/MIDAS northern summer program. *Geophys. Res. Lett.*, *31*(24), L24S03. https://doi.org/10.1029/2004GL019615

Becker, E., and Fritts, D. C. (2006). Enhanced gravity-wave activity and interhemispheric coupling during the MaCWAVE/MIDAS northern summer program 2002. *Ann. Geophysi.*, *24*(4), 1175–1188. https://doi.org/10.5194/angeo-24-1175-2006

Becker, E., and Vadas, S. L. (2018). Secondary gravity waves in the winter mesosphere: Results from a high-resolution global circulation model. *J. Geophys. Res.: Atmos.*, *123*(5), 2605–2627. https://doi.org/10.1002/2017JD027460

Chandran, A., Collins, R. L., and Harvey, V. L. (2014). Stratosphere-mesosphere coupling during stratospheric sudden warming events. *Adv. Space Res.*, *53*(9), 1265–1289. https://doi.org/10.1016/j.asr.2014.02.005

Dunkerton, T. (1978). On the mean meridional mass motions of the stratosphere and mesosphere. *J. Atmos. Sci.*, *35*(12), 2325–2333. https://doi.org/10.1175/1520-0469(1978)035<2325:OTMMMM>2.0.CO;2

Dvinskikh, N. I. (1988). Expansion of ionospheric characteristics fields in empirical orthogonal functions. *Adv. Space Res.*, *8*(4), 179–187. https://doi.org/10.1016/0273-1177(88)90238-4

Ern, M., Preusse, P., Kalisch, S., Kaufmann, M., and Riese, M. (2013). Role of gravity waves in the forcing of quasi two-day waves in the mesosphere: An observational study. *J. Geophys. Res.: Atmos.*, *118*(9), 3467–3485. https://doi.org/10.1029/2012JD018208

France, J. A., Randall, C. E., Lieberman, R. S., Harvey, V. L., Eckermann, S. D., Siskind, D. E., Lumpe, J. D., Bailey, S. M., Carstens, J. N., and Russell III, J. M. (2018). Local and remote planetary wave effects on polar mesospheric clouds in the northern hemisphere in 2014. *J. Geophys. Res.: Atmos.*, *123*(10), 5149–5162. https://doi.org/10.1029/2017JD028224

Fritts, D. C., and Alexander, M. J. (2003). Gravity wave dynamics and effects in the middle atmosphere. *Rev. Geophys.*, *41*(1), 1003. https://doi.org/10.1029/2001RG000106

Gu, S. Y., Liu, H. L., Pedatella, N. M., Dou, X. K., Li, T., and Chen, T. D. (2016a). The quasi 2 day wave activities during 2007 austral summer period as revealed by whole atmosphere community climate model. *J. Geophys. Res.: Space Phys.*, *121*(3), 2743–2754. https://doi.org/10.1002/2015JA022225

Gu, S. Y., Liu, H. L., Pedatella, N. M., Dou, X. K., and Shu, Z. F. (2016b). The quasi-2 day wave activities during 2007 boreal summer period as revealed by Whole Atmosphere Community Climate Model. *J. Geophys. Res.: Space Phys.*, *121*(7), 7256–7268. https://doi.org/10.1002/2016JA022867

Gumbel, J., and Karlsson, B. (2011). Intra-and inter-hemispheric coupling effects on the polar summer mesosphere. *Geophys. Res. Lett.*, *38*(14), L14804. https://doi.org/10.1029/2011GL047968

Haynes, P. H., Mcintyre, M. E., Shepherd, T. G., Marks, C. J., and Shine, K. P. (1991). On the "downward control" of extratropical diabatic circulations by eddy-induced mean zonal forces. *J. Atmos. Sci.*, *48*(4), 651–678. https://doi.org/10.1175/1520-0469(1991)048<0651:OTCOED>2.0.CO;2

Holton, J. R. (1983). The influence of gravity wave breaking on the general circulation of the middle atmosphere. *J. Atmos. Sci.*, *40*(10), 2497–2507. https://doi.org/10.1175/1520-0469(1983)040<2497:TIOGWB>2.0.CO;2

Holton, J. R., and Alexander, M. J. (2000). The role of waves in the transport circulation of the middle atmosphere. In D. E. Siskind (Ed.), *Geophysical Monograph Series*. Washington, DC: American Geophysical Union. https://doi.org/10.1029/GM123p0021

Jolliffe, I. T. (2002). *Principal Component Analysis for Special Types of Data*. New York: Springer. https://doi.org/10.1007/0-387-22440-8_13

Karlsson, B., Körnich, H., and Gumbel, J. (2007). Evidence for interhemispheric stratosphere-mesosphere coupling derived from noctilucent cloud properties. *Geophys. Res. Lett.*, *34*(16), L16806. https://doi.org/10.1029/2007GL030282

Karlsson, B., McLandress, C., and Shepherd, T. G. (2009a). Inter-hemispheric mesospheric coupling in a comprehensive middle atmosphere model. *J. Atmos. Solar-Terrestr. Phys.*, *71*(3-4), 518–530. https://doi.org/10.1016/j.jastp.2008.08.006

Karlsson, B., Randall, C. E., Benze, S., Mills, M., Harvey, V. L., Bailey, S. M., and Russell III, J. M. (2009b). Intra-seasonal variability of polar mesospheric clouds due to inter-hemispheric coupling. *Geophys. Res. Lett.*, *36*(20), L20802. https://doi.org/10.1029/2009GL040348

Karlsson, B., and Becker, E. (2016). How does interhemispheric coupling contribute to cool down the summer polar mesosphere?. *J. Climate*, *29*(24), 8807–8821. https://doi.org/10.1175/JCLI-D-16-0231.1

Körnich, H., and Becker, E. (2010). A simple model for the interhemispheric coupling of the middle atmosphere circulation. *Adv. Space Res.*, *45*(5), 661–668. https://doi.org/10.1016/j.asr.2009.11.001

Koshin, D., and Sato, K. (2024). Characteristics and mechanism of interhemispheric coupling in austral winter revealed by long-term reanalysis data for the whole middle atmosphere. *J. Geophys. Res.: Atmos.*, *129*(1), e2023JD039687. https://doi.org/10.1029/2023JD039687

Iimura, H., Fritts, D. C., Lieberman, R. S., Janches, D., Mitchell, N. J., Franke, S. J., Singer, W., Hocking, W. K., Taylor, M. J., and Moffat-Griffin, T. (2021). Climatology of quasi-2-day wave structure and variability at middle latitudes in the northern and southern hemispheres. *Journal of Atmospheric and Solar-Terrestrial Physics*, *221*, 105690. https://doi.org/10.1016/j.jastp.2021.105690

Limpasuvan, V., Richter, J. H., Orsolini, Y. J., Stordal, F., and Kvissel, O. K. (2012). The roles of planetary and gravity waves during a major stratospheric sudden warming as characterized in WACCM. *J. Atmos. Solar-Terrestr. Phys.*, *78–79*, 84–98. https://doi.org/10.1016/j.jastp.2011.03.004

Liu, H. L., Talaat, E. R., Roble, R. G., Lieberman, R. S., Riggin, D. M., and Yee, J. H. (2004). The 6.5-day wave and its seasonal variability in the middle and upper atmosphere. *J. Geophys. Res.: Atmos.*, *109*(D21), D21112. https://doi.org/10.1029/2004JD004795

Liu, H. L., Foster, B. T., Hagan, M. E., McInerney, J. M., Maute, A., Qian, L., Richmond, A. D., Roble, R. G., Solomon, S. C., Garcia, R. R., … Oberheide, S. J. (2010). Thermosphere extension of the whole atmosphere community climate model. *J. Geophys. Res.: Space Phys.*, *115*(A12), A12302. https://doi.org/10.1029/2010ja015586

Liu, H. L., Bardeen, C. G., Foster, B. T., Lauritzen, P., Liu, J., Lu, G., Marsh, D. R., Maute, A., Mcinerney, J. M., … Wang, W. B. (2018). Development and validation of the whole atmosphere community climate model with thermosphere and ionosphere extension (WACCM-X 2.0). *J. Adv. Model. Earth Syst.*, *10*(2), 381–402. https://doi.org/10.1002/2017ms001232

Liu, J. B., Hernandez-Pajares, M., Liang, X. L., An, J. C., Wang, Z. M., Chen, R. Z., Sun, W., and Hyyppä, J. (2017). Temporal and spatial variations of global ionospheric total electron content under various solar conditions. *J. Geod.*, *91*(5), 485–502. https://doi.org/10.1007/s00190-016-0977-7

Manney, G. L., Zurek, R. W., O'Neill, A., and Swinbank, R. (1994). On the motion of air through the stratospheric polar vortex. *J. Atmos. Sci.*, *51*(20), 2973–2994. https://doi.org/10.1175/1520-0469(1994)051<2973:OTMOAT>2.0.CO;2

Marsh, D. R. (2011). Chemical–Dynamical coupling in the mesosphere and lower thermosphere. In: M. Ali Abdu et al. (Eds.), *Aeronomy of the Earth's Atmosphere and Ionosphere* (pp. 3–17). Netherlands: Springer. https://doi.org/10.1007/978-94-007-0326-1_1

McLandress, C., Ward, W. E., Fomichev, V. I., Semeniuk, K., Beagley, S. R., Mcfarlane, N. A., and Shepherd, T. G. (2006). Large-scale dynamics of the mesosphere and lower thermosphere: An analysis using the extended Canadian Middle Atmosphere Model. *J. Geophys. Res.: Atmos.*, *111*(D17), D17111. https://doi.org/10.1029/2005JD006776

Pendlebury, D. (2012). A simulation of the quasi-two-day wave and its effect on variability of summertime mesopause temperatures. *J. Atmos. Solar-Terrestr. Phys.*, *80*, 138–151. https://doi.org/10.1016/j.jastp.2012.01.006

Plumb, R. A. (1983). Baroclinic instability of the summer mesosphere: A mechanism for the quasi-two-day wave?. *J. Atmos. Sci.*, *40*(1), 262–270. https://doi.org/10.1175/1520-0469(1983)040<0262:BIOTSM>2.0.CO;2

Qin, Y. S., Gu, S. Y., Teng, C. K. M., Dou, X. K., Yu, Y., and Li, N. (2021). Comprehensive study of the climatology of the Quasi-6-day wave in the MLT region based on Aura/MLS observations and SD-WACCM-X simulations. *J. Geophys. Res.: Space Phys.*, *126*(1), e2020JA028454. https://doi.org/10.1029/2020JA028454

Rodgers, C. D., and Prata, A. J. (1981). Evidence for a traveling two-day wave in the middle atmosphere. *J. Geophys. Res.: Oceans*, *86*(C10), 9661–9664. https://doi.org/10.1029/JC086iC10p09661

Sassi, F., Liu, H. L., Ma, J., and Garcia, R. R. (2013). The lower thermosphere during the northern hemisphere winter of 2009: A modeling study using high-altitude data assimilation products in WACCM-X. *J. Geophys. Res.: Atmos.*, *118*(16), 8954–8968. https://doi.org/10.1002/jgrd.50632

Sato, K., and Nomoto, M. (2015). Gravity wave–induced anomalous potential vorticity gradient generating planetary waves in the winter mesosphere. *J. Atmos. Sci.*, *72*(9), 3609–3624. https://doi.org/10.1175/JAS-D-15-0046.1

Siskind, D. E., Stevens, M. H., Hervig, M., Sassi, F., Hoppel, K., Englert, C. R., and Kochenash, A. J. (2011). Consequences of recent Southern Hemisphere winter variability on polar mesospheric clouds. *J. Atmos. Solar-Terrestr. Phys.*, *73*(13), 2013–2021. https://doi.org/10.1016/j.jastp.2011.06.014

Siskind, D. E., and McCormack, J. P. (2014). Summer mesospheric warmings and the quasi 2 day wave. *Geophys. Res. Lett.*, *41*(2), 717–722. https://doi.org/10.1002/2013GL058875

Smith, A. K., Pedatella, N. M., and Mullen, Z. K. (2020). Interhemispheric coupling mechanisms in the middle atmosphere of WACCM6. *J. Atmos. Sci.*, *77*(3), 1101–1118. https://doi.org/10.1175/JAS-D-19-0253.1

Smith, A. K., Pedatella, N. M., and Bardeen, C. G. (2022). Global middle-atmosphere response to winter stratospheric variability in SABER and MLS mean temperature. *J. Atmos. Sci.*, *79*(6), 1727–1741. https://doi.org/10.1175/JAS-D-21-0259.1

Wan, W. X., Ding, F., Ren, Z. P., Zhang, M. L., Liu, L. B., and Ning, B. Q. (2012). Modeling the global ionospheric total electron content with empirical orthogonal function analysis. *Sci. China Technol. Sci.*, *55*(5), 1161–1168. https://doi.org/10.1007/s11431-012-4823-8

Yasui, R., Sato, K., and Miyoshi, Y. (2018). The momentum budget in the stratosphere, mesosphere, and lower thermosphere. Part II: the in situ generation of gravity waves. *J. Atmos. Sci.*, *75*(10), 3635–3651. https://doi.org/10.1175/JAS-D-17-0337.1

Yulaeva, E., Holton, J. R., and Wallace, J. M. (1994). On the cause of the annual cycle in tropical lower-stratospheric temperatures. *J. Atmos. Sci.*, *51*(2), 169–174. https://doi.org/10.1175/1520-0469(1994)051<0169:OTCOTA>2.0.CO;2

Yasui, R., Sato, K., and Miyoshi, Y. (2021). Roles of Rossby waves, Rossby–Gravity waves, and Gravity waves generated in the middle atmosphere for interhemispheric coupling. *J. Atmos. Sci.*, *78*(12), 3867–3888. https://doi.org/10.1175/JAS-D-21-0045.1